Micro and Nanostructures 216 (2026) 208714

Contents lists available at ScienceDirect

Micro and Nanostructures

journal homepage: www.journals.elsevier.com/micro-and-nanostructures

Interplay of composition, crystallinity, and chemical structure in CoHCF and NiHCF thin films prepared at different temperatures

Larissa de O. Garcia [a,*], Michael Pohlitz [a], Mohammed F. Kalady [b], Christian K. Müller [a]

[a] Faculty of Physical Engineering/Computer Sciences, University of Applied Sciences Zwickau, Zwickau, 08056, Germany
[b] Leibniz Institute for Solid State and Materials Research Dresden (IFW Dresden), Dresden, 01069, Germany

ARTICLE INFO

Keywords:
Prussian blue analogues
Electrodeposition
Crystal chemistry
Defects
Temperature

ABSTRACT

Understanding how growth conditions govern structural order and ion transport in Prussian blue analogues (PBAs) thin films is essential for optimizing their electrochemical performance. Here, cobalt and nickel hexacyanoferrate (CoHCF and NiHCF) thin films were electrodeposited potentiostatically at temperatures between 20 and 60 °C. A combination of cyclic voltammetry, scanning electron microscopy, X-ray diffraction, and Raman spectroscopy was employed to elucidate the interplay between composition, crystallinity, and chemical structure.

Under identical conditions, CoHCF exhibits a maximum current density approximately 2.2 times higher than NiHCF, indicating significantly faster electrochemical kinetics. X-ray diffraction reveals temperature-dependent lattice expansion without phase transitions, with a maximum near 40 °C, associated with structural relaxation and compositional variations. Raman spectroscopy further reveals temperature-dependent local structural evolution, where cyanide band narrowing at intermediate temperatures indicates improved short-range order, while band broadening at higher temperatures reflects increased defect density.

These findings demonstrate that temperature-controlled defect redistribution governs both short- and long-range structural order in PBA thin films, directly influencing ion transport and electrochemical response. This work provides new insights into structure–property relationships and establishes deposition temperature as a key parameter for tuning electrochemical functionality in hexacyanoferrate-based electrodes.

1. Introduction

Prussian blue analogues (PBAs) constitute a versatile class of coordination polymers formed by cyanide-bridged transition-metal ions, exhibiting open framework structures, rich redox chemistry, and remarkable compositional flexibility [1]. Owing to these characteristics, PBAs have attracted considerable attention for applications in electrochemical energy storage [2], electrocatalysis [3], and sensing technologies [4]. In particular, cobalt- and nickel-based hexacyanoferrates (CoHCF and NiHCF) have emerged as promising candidates due to their chemical stability, tunable electronic properties, strong sensitivity to chemical composition and defect chemistry, making them ideal platforms for investigating structure–property relationships in cyanide-bridged frameworks [5–7].

The functional properties of PBAs are governed by both local and long-range structural order. Parameters such as chemical composition, alkali-metal content, and the concentration of $[Fe(CN)_6]$ vacancies directly influence lattice parameters, electronic

* Corresponding author.
E-mail address: larissa.de.oliveira.garcia@whz.de (L.d.O. Garcia).
URL: https://orcid.org/0000-0003-0267-6488 (L.d.O. Garcia).

https://doi.org/10.1016/j.micrna.2026.208714
Received 17 March 2026; Received in revised form 10 April 2026; Accepted 22 April 2026
Available online 2 May 2026
2773-0123/© 2026 The Authors. Published by Elsevier Ltd. This is an open access article under the CC BY license (http://creativecommons.org/licenses/by/4.0/).

structure, ionic transport, and vibrational properties [8,9]. Additionally, coordinated and interstitial water species affect local bonding environments and charge-compensation mechanisms, thereby influencing redox activity and lattice dynamics. Consequently, even subtle variations in composition and defect chemistry can induce pronounced changes in the functional response of PBAs [10,11].

When processed as thin films, these structure–property relationships become more complex. Reduced dimensionality, substrate–film interactions, and kinetically controlled growth conditions can stabilize non-equilibrium structures that differ significantly from their bulk counterparts [12,13]. As a result, thin-film PBAs often exhibit enhanced defect densities, compositional heterogeneity, and anisotropic structural order, all of which are critical for applications requiring controlled ion transport, stable electrochemical behavior, and well-defined interfacial properties [14,15]. Despite their technological relevance, systematic studies addressing how synthesis parameters govern defect formation and compositional variation in PBA thin films remain limited.

Among the synthesis parameters, temperature plays a central role in determining crystallinity, morphology, and defect landscapes in PBAs [16]. At low temperatures, limited atomic mobility typically results in reduced crystallinity, small grain sizes, and increased structural disorder [17]. Increasing temperature enhances atomic diffusion and long-range ordering but may simultaneously promote alkali-ion incorporation, vacancy formation, and the retention of framework water [18]. This introduces a trade-off between improved crystallinity and defect generation, which remains insufficiently understood in electrodeposited PBA thin films [19,20].

Defects in PBAs are increasingly recognized not merely as imperfections but as key parameters governing ionic transport and electrochemical response [21]. Vacancies and local structural distortions can facilitate ion diffusion and modulate redox processes, whereas excessive disorder may compromise structural stability [22,23]. Establishing direct correlations between structural evolution and electrochemical behavior is therefore essential for rational materials design. In this context, cyclic voltammetry provides insight into redox activity, charge-transfer kinetics, and ion accessibility in PBA frameworks [24,25], while Raman spectroscopy serves as a sensitive probe of local structural order. In particular, the C≡N stretching modes respond strongly to metal–ligand coordination, oxidation state, and symmetry, enabling the detection of local disorder and compositional variations that may not be captured by diffraction techniques [26,27].

Despite previous studies on the temperature-dependent growth of PBAs in bulk systems, the systematic correlation between deposition temperature, local structural disorder, and electrochemical behavior in electrodeposited thin films remains largely unexplored. The interplay between composition, defect distribution, and multiscale structural ordering, in particular, has not been comprehensively addressed. In this study, we systematically investigate CoHCF and NiHCF thin films electrodeposited at temperatures between 20 and 60 °C. Using a combination of cyclic voltammetry (CV), X-ray diffraction (XRD), scanning electron microscopy (SEM), and Raman spectroscopy, we establish a direct correlation between deposition temperature, structural evolution, and electrochemical performance. Our results reveal a non-monotonic relationship between crystallinity and electrochemical activity. This demonstrates that defect-mediated structural dynamics play a dominant role in governing ion transport. Furthermore, a comparative analysis of Co- and Ni-based hexacyanoferrates highlights the role of the transition-metal center in modulating structural flexibility and defect sensitivity. These findings provide new insights into temperature-controlled structure–property relationships in PBA thin films and offer practical guidelines for the rational design of cyanide-bridged materials with tailored electrochemical functionality.

2. Materials and methods

2.1. Sample preparation

Prussian blue analogues (PBAs) thin films were prepared by potentiostatic electrodeposition using a conventional three-electrode electrochemical cell. A platinum plate served as the counter electrode, a saturated calomel electrode (SCE) as the reference electrode, and Au (50 nm)/Cr (5 nm) layers deposited on Si (100) substrates as the working electrode. Electrochemical deposition was carried out using an Ivium CompactStat potentiostat (Ivium Technologies, Eindhoven, The Netherlands). All potentials reported in this work are referenced to the SCE.

Film growth was performed at a constant applied potential of 0.30 V until a total charge of 50 mC was reached. The effective deposition area (approximately 0.5 cm^2) was defined using an adhesive mask applied to the working electrode surface. The electrolyte consisted of an aqueous solution containing 1.0 M KCl, 0.25 mM $K_3Fe(CN)_6$, and 0.25 mM metal chloride precursor. The pH was adjusted to approximately 2 by the addition of hydrochloric acid. All chemicals were of analytical grade and used as received. The electrodeposition procedure followed protocols previously established by our group [28,29].

During deposition, the electrolyte temperature was controlled using a thermostated water bath and continuously monitored with a calibrated thermometer. The deposition temperature was varied between 20 and 60 °C. This configuration ensured thermal homogeneity of the electrolyte and minimized temperature gradients at the electrode surface during film growth.

Following the nomenclature adopted in our previous work [29], the deposited films were labeled according to the transition metal precursor: CoHCF for cobalt hexacyanoferrate films and NiHCF for nickel hexacyanoferrate films.

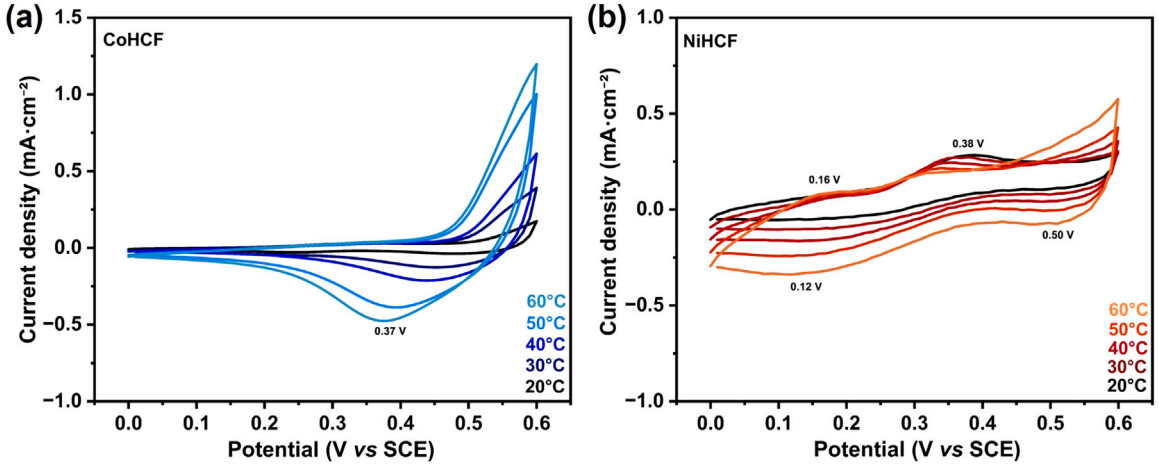


Fig. 1. Cyclic voltammograms of (a) CoHCF and (b) NiHCF recorded at different temperatures (20–60 °C) in 1.0 M KCl aqueous electrolyte at a scan rate of 100 mV s^{-1}.

2.2. Material characterization

Structural characterization was performed by X-ray diffraction (XRD) using an X'Pert MRD diffractometer (PANalytical, Almelo, The Netherlands) with Co Kα radiation (λ = 1.78896 Å). Measurements were carried out in Bragg–Brentano geometry over a 2θ range of 10–40° with a step size of 0.005°.

Morphological and compositional analyses were conducted using a field-emission scanning electron microscope (FEG-SEM, TESCAN CLARA, Brno, Czech Republic) equipped with an energy-dispersive X-ray spectroscopy (EDS) detector (Ultim Max 65 SDD, Oxford Instruments, Wiesbaden, Germany). SEM imaging and EDS measurements were performed at an accelerating voltage of 20 kV.

Raman spectroscopy was carried out using a confocal Raman system (WITec RISE, Ulm, Germany) with a 532 nm excitation laser. To avoid local heating and sample degradation, the laser power was limited to 0.4 mW for all measurements.

Electrochemical characterization was performed by cyclic voltammetry (CV) using the same three-electrode configuration described above. Measurements were conducted in a 1.0 M KCl aqueous electrolyte within a potential window of 0.0–0.6 V at a scan rate of 100 mV s^{-1}. All potentials are reported with respect to the SCE.

3. Results and discussion

3.1. Electrochemical characterization

The electrochemical behavior of CoHCF and NiHCF thin films was investigated by cyclic voltammetry (CV) in a 1.0 M KCl aqueous electrolyte within a potential window of 0.0–0.6 V vs SCE at temperatures ranging from 20 to 60 °C (Fig. 1). This potential range was selected to avoid irreversible oxidation processes and to ensure structural stability during cycling. The upper potential limit was further restricted to isolate the dominant Fe^{2+}/Fe^{3+} redox process associated with K^+ insertion/extraction, while minimizing contributions from secondary reactions [29].

Both materials exhibit reversible redox features characteristic of Prussian blue analogues (PBAs), in which Fe-centered redox reactions are coupled to alkali-ion transport within an open cyanide-bridged framework [30–32]. The electrochemical response was highly reproducible across multiple samples.

For CoHCF (Fig. 1(a)), a well-defined cathodic peak centered at approximately 0.37 V vs SCE is observed, accompanied by a corresponding anodic peak at higher potentials. Increasing temperature results in a systematic increase in current density and progressive sharpening of the redox peaks. At 60 °C, CoHCF reaches a maximum cathodic current density of approximately 1.2 mA cm^{-2}, indicating an enhanced electrochemical response under elevated temperature conditions.

In contrast, NiHCF (Fig. 1(b)) exhibits broader redox features distributed over a wider potential window (approximately 0.12–0.50 V vs SCE), indicating the presence of multiple local redox environments rather than a single well-defined transition [33]. At 60 °C, the maximum cathodic current density reaches approximately 0.55 mA cm^{-2}. A quantitative comparison based on the maximum cathodic peak current at 60 °C shows that CoHCF exhibits a current density approximately 2.2 times higher than NiHCF under identical conditions. This difference provides experimental evidence of enhanced electrochemical kinetics in CoHCF.

The temperature-dependent increase in current density and peak sharpening observed for both materials indicates thermally activated electrochemical behavior, consistent with enhanced ionic mobility and reduced kinetic limitations at elevated temperatures. In CoHCF, the sharper and more intense peaks suggest a more uniform electrochemical response and improved ion accessibility

Table 1
Comparison of electrochemical performance of hexacyanoferrate-based materials reported in literature and in this work.

Material	Synthesis method	Current density (mA cm^{-2})	Electrolyte/Ion	Key feature	Ref
CoHCF (this work)	Electrodeposition	~1.2	KCl/K^+	Temperature-controlled electrochemical response; maximum at 60 °C	This work
NiHCF (this work)	Electrodeposition	~0.55	KCl/K^+	Broader redox features; disorder-sensitive response	This work
CoHCF	Electrodeposition	0.5–1.0	–/K^+	Electrocatalytic enhancement with Au co-deposition	[32]
NiHCF	Cathodic thin film	0.2–0.6	–/K^+	Structural disorder governs electrochemical response	[33]
NiHCF	Chemical (aqueous)	~0.8	KNO_3/K^+	Improved ion transport in nanostructured films	[39]
Co/Ni PBA	Composite	1.0–2.0	–	Synergistic electrochemical enhancement	[25]

within the framework. In contrast, the broader response observed in NiHCF reflects a distribution of redox sites, typically associated with structural disorder, vacancy distribution, and compositional heterogeneity [34,35].

Although electrochemical impedance spectroscopy would be required for a quantitative separation of charge-transfer resistance and diffusion contributions, the consistent trends observed in cyclic voltammetry (CV), together with structural and spectroscopic analyses (scanning electron microscopy (SEM), X-ray diffraction (XRD), and Raman spectroscopy), indicate that the electrochemical response is governed by coupled ionic transport and interfacial processes.

In both systems, the electrochemical behavior is dominated by the reversible Fe^{2+}/Fe^{3+} redox couple associated with K^+ insertion/extraction, while Co^{2+} and Ni^{2+} primarily act as structural centers without distinct redox activity within the investigated potential window [30,31,36]. These electrochemical reactions can be described by the following equilibria for CoHCF [32,37]:

$$K\mathrm{Co}^{\mathrm{II}}_{1.5}[\mathrm{Fe}^{\mathrm{II}}(\mathrm{CN})_6] \rightleftharpoons \mathrm{Co}^{\mathrm{II}}_{1.5}[\mathrm{Fe}^{\mathrm{III}}(\mathrm{CN})_6] + K^+ + e^- \quad (1)$$

$$K_2\mathrm{Co}^{\mathrm{II}}[\mathrm{Fe}^{\mathrm{II}}(\mathrm{CN})_6] \rightleftharpoons K\mathrm{Co}^{\mathrm{II}}[\mathrm{Fe}^{\mathrm{III}}(\mathrm{CN})_6] + K^+ + e^- \quad (2)$$

An analogous mechanism can be applied to NiHCF, where the Fe^{2+}/Fe^{3+} couple similarly dominates the electrochemical response. The coexistence of these configurations is closely linked to the presence of $[Fe(CN)_6]$ vacancies and coordinated water molecules, which introduce local structural distortions and a distribution of redox potentials [34,35,38]. These effects are consistent with the broader electrochemical features observed, particularly for NiHCF.

A comparison with literature data (Table 1) indicates that the current densities obtained here fall within the typical range reported for hexacyanoferrate-based thin films. The differences observed between CoHCF and NiHCF are primarily attributed to variations in structural ordering and defect distribution induced by deposition temperature, rather than to significant differences in metal-centered redox activity within the investigated potential window.

Importantly, these results indicate that the distinct electrochemical behavior of CoHCF and NiHCF arises primarily from differences in framework rigidity, defect chemistry, and ion-transport pathways, rather than intrinsic differences in metal-centered redox activity, as discussed in the following sections.

3.2. Morphological characterization by SEM and EDS

To elucidate the structural origins of the distinct electrochemical behavior observed for CoHCF and NiHCF, their morphology and microstructure were investigated by scanning electron microscopy (SEM) (Fig. 2). As electrodeposition was performed within the electrochemically active Fe^{2+}/Fe^{3+} redox regime, the resulting morphologies reflect kinetically controlled growth conditions governed by the interplay between nucleation and crystal growth.

For both materials, a clear evolution of surface morphology with deposition temperature is observed, highlighting the role of temperature in governing growth processes. Increasing temperature enhances surface diffusion and reduces kinetic barriers, thereby promoting crystallite growth and coalescence [40,41].

However, the extent of this effect differs significantly between the two systems. CoHCF films (Fig. 2(a)) exhibit relatively large and well-defined faceted crystallites across the entire temperature range, indicating a predominantly growth-controlled deposition regime. Only minor morphological variations are observed between 20 °C and 60 °C. At 20 °C, the films already display well-developed faceted grains, while at 60 °C a slight increase in crystallite size and improved inter-grain connectivity are observed.

This comparatively weak temperature dependence suggests a kinetically favorable growth regime that is less sensitive to thermal variations. Such behavior is consistent with stronger metal–ligand interactions and higher framework rigidity in Co-based PBAs, which favor structural stability and long-range ordering [34,35].

Although no statistical grain size analysis was performed, the observed morphological features were consistent across multiple regions and independently prepared samples, supporting the reproducibility of the trends discussed.

In contrast with CoHCF, NiHCF films (Fig. 2(b)) exhibit a pronounced temperature dependence. At 20 °C, the films display an inhomogeneous morphology with visible cracks and poorly connected grains, indicative of limited surface diffusion and nucleation-dominated growth. At intermediate temperatures (30–40 °C), the morphology evolves into dense and more homogeneous granular

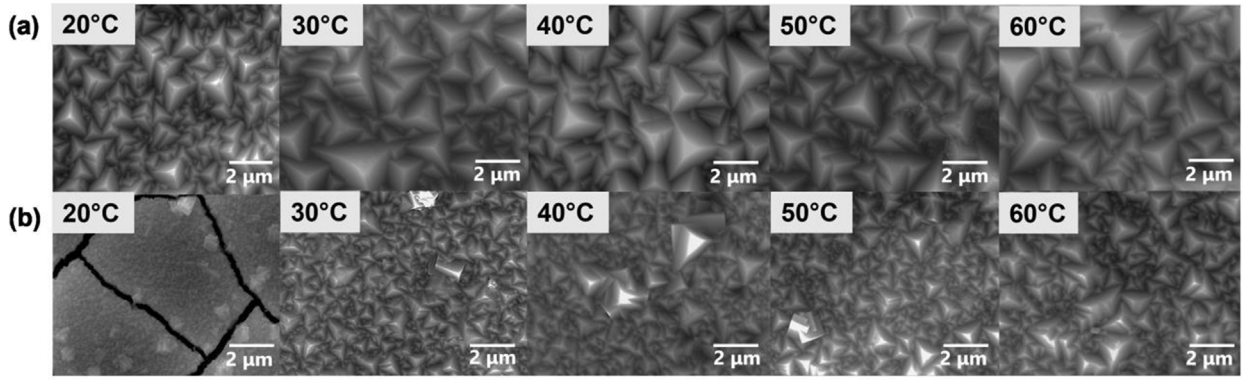


Fig. 2. SEM images of (a) CoHCF and (b) NiHCF thin films electrodeposited at different temperatures (20–60 °C).

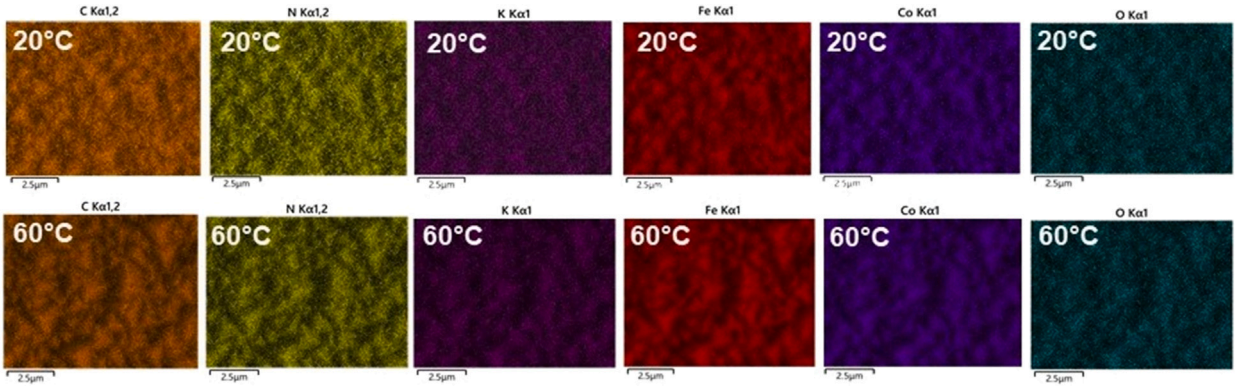


Fig. 3. EDX elemental mapping of CoHCF thin films electrodeposited at 20 and 60 °C.

structures, reflecting increased nucleation density and enhanced surface mobility. At higher temperatures (50–60 °C), significant grain growth and coalescence occur, leading to larger aggregates and improved film continuity. This transition from nucleation-limited to growth-dominated regimes highlights the stronger sensitivity of NiHCF to deposition temperature. The improved homogeneity observed at intermediate temperatures is consistent with the reduced electrochemical polarization and enhanced current response observed in CV measurements.

Elemental composition and spatial distribution were further examined by energy-dispersive X-ray spectroscopy (EDS). Representative elemental maps for films deposited at 20 and 60 °C are shown in Figs. 3 and 4, while additional maps for intermediate temperatures are provided in the Supplementary Information. For both materials and all investigated temperatures, the EDS maps confirm a homogeneous spatial distribution of the constituent elements, with no evidence of segregation or secondary phase formation.

Semi-quantitative EDS analysis of CoHCF and NiHCF films (Tables 2 and 3) confirms the presence of potassium and oxygen, reflecting the incorporation of K^+ ions for charge compensation and the presence of coordinated and/or interstitial water molecules.

It should be noted that EDS measurements probe near-surface composition and may be influenced by interaction volume effects as well as possible substrate contributions. In addition, absolute atomic percentages should be interpreted with caution due to the limitations of EDS in light-element quantification; however, the observed trends provide reliable comparative information across the temperature series.

A systematic dependence of the O/K ratio on deposition temperature is observed for both materials. In general, increasing temperature promotes higher potassium incorporation and a relative decrease in oxygen content. For CoHCF, the K content increases from 7.36 at.% at 20 °C to 9.82 at.% at 60 °C, while the O content decreases from 6.82 to 4.82 at.%. A similar trend is observed for NiHCF, where the K content increases from 5.30 to 8.22 at.%, whereas the O content varies within a narrower range between 4.27 and 5.05 at.%.

These trends suggest temperature-dependent changes in the balance between alkali-ion incorporation and hydration within the framework. Although EDS does not directly quantify vacancy concentration, the observed variations are consistent with modifications in defect distribution and coordinated water content.

Independent evidence of the chemical states and composition of CoHCF and NiHCF thin films has been reported in our previous work [29], where X-ray photoelectron spectroscopy (XPS) confirmed the presence of Co^{2+}, Ni^{2+}, and mixed Fe^{2+}/Fe^{3+} oxidation

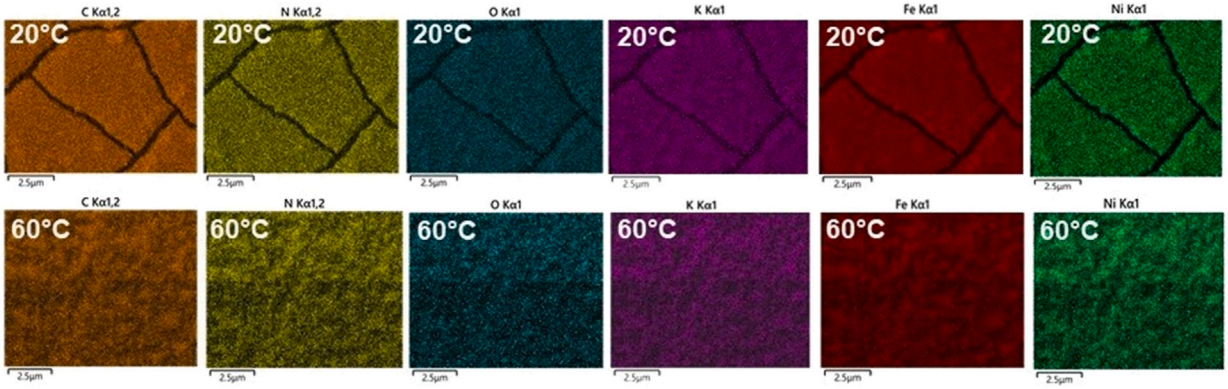


Fig. 4. EDX elemental mapping of NiHCF thin films electrodeposited at 20 and 60 °C.

Table 2
Elemental composition (at.%) of CoHCF thin films obtained by EDS mapping at different deposition temperatures.

Temperature (°C)	C	N	K	O	Fe	Co
20	41.12	36.01	7.36	6.82	4.22	4.46
30	37.84	35.14	8.69	8.04	5.00	5.28
40	39.38	35.25	9.36	5.78	5.08	5.15
50	39.56	35.88	9.32	5.07	5.13	5.05
60	39.45	35.36	9.82	4.82	5.42	5.13

Table 3
Elemental composition (at.%) of NiHCF thin films obtained by EDS mapping at different deposition temperatures.

Temperature (°C)	C	N	K	O	Fe	Ni
20	43.77	39.60	5.30	4.27	3.31	3.75
30	41.87	37.57	7.23	4.90	4.32	4.11
40	41.73	37.44	7.59	4.51	4.34	4.39
50	40.41	37.94	7.20	5.72	4.98	3.74
60	40.20	37.47	8.22	5.05	4.80	4.27

states. These results support the compositional interpretation presented here and further validate the use of EDS for comparative analysis across the temperature series.

Such compositional changes are expected to influence both lattice parameters and local structural environments, in agreement with the XRD and Raman results. Increased potassium incorporation may partially compensate framework vacancies, while variations in oxygen content are associated with changes in coordinated and/or interstitial water. Together, these factors modify the local bonding environment and contribute to the structural stability of the PBA framework.

Taken together, the combined morphological and compositional analyses reveal distinct growth mechanisms for CoHCF and NiHCF under identical deposition conditions. CoHCF exhibits a relatively stable, growth-dominated morphology with weak temperature dependence, whereas NiHCF undergoes a clear transition from nucleation-controlled to growth-controlled regimes as temperature increases. These differences influence structural ordering and defect distribution, providing a consistent and unified interpretation of the temperature-dependent trends observed across XRD, Raman, and electrochemical measurements.

3.3. Structural characterization by X-ray diffraction

X-ray diffraction (XRD) was employed to investigate the crystallographic structure and lattice evolution of CoHCF and NiHCF thin films as a function of deposition temperature. In Prussian blue analogues (PBAs), the lattice structure is highly sensitive to alkali-ion occupancy, $[Fe(CN)_6]$ vacancies, and local structural distortions within the metal–cyanide framework. These factors can induce measurable deviations from ideal cubic symmetry and significantly influence long-range structural order [34,35,38]. Consequently, the temperature-dependent compositional variations identified by EDS are expected to impact both lattice parameters and structural ordering.

The XRD patterns collected in the 2θ range of 10–40° are shown in Fig. 5. This angular range emphasizes the characteristic reflections of the PBA framework while minimizing contributions from the Au/Cr substrate, whose most intense peaks occur at higher diffraction angles [42,43]. The dominant reflections observed at approximately 17°, 24°, 35°, and 39° correspond to the (111), (220), (222), and (400) planes, respectively, consistent with a face-centered cubic structure (space group $Fm\bar{3}m$).

To facilitate phase identification, reference stick patterns corresponding to the cubic PBA structure were included in Fig. 5, based on standard diffraction data from the ICDD database (PDF No. 01-0239). The reference data were adapted to Co Kα radiation to

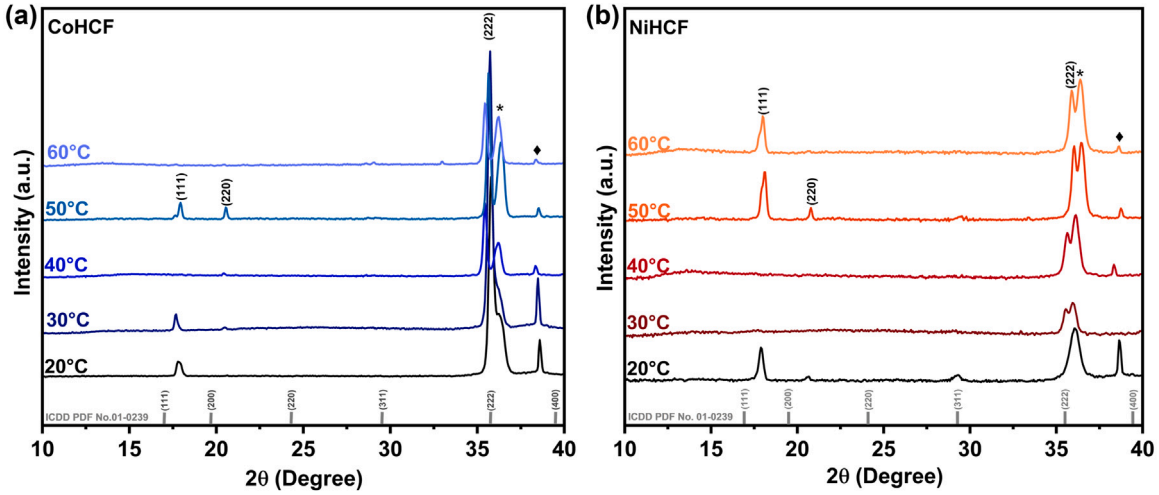


Fig. 5. X-ray diffraction (XRD) patterns of (a) CoHCF and (b) NiHCF thin films electrodeposited at different temperatures (20–60 °C). Reflections marked with asterisks (*) are associated with structural disorder, while diamond symbols (♦) indicate the presence of a surface oxide layer. Reference stick patterns corresponding to the cubic Prussian blue analogue structure (space group $Fm\bar{3}m$, ICDD PDF No. 01-0239) were adapted to Co Kα radiation and are shown at the bottom of each panel for comparison.

match the experimental conditions. Although the original ICDD data are typically reported for Cu Kα radiation, this conversion preserves the relative peak positions and crystallographic indexing, enabling direct comparison with the experimental patterns.

A clear evolution of peak intensity and sharpness with deposition temperature is observed for both materials. For CoHCF (Fig. 5(a)), relatively well-defined reflections are obtained at intermediate temperatures, while partial peak broadening and intensity reduction occur at 40 and 60 °C. Similarly, NiHCF (Fig. 5(b)) exhibits broader and less intense reflections, particularly at 30 and 40 °C. These features indicate a reduction in long-range structural coherence and an increase in structural disorder.

The observed peak broadening and intensity variations are attributed to temperature-dependent structural disorder, including defect formation, lattice strain, and finite crystallite size effects, rather than to the formation of secondary crystalline phases. This interpretation is supported by the absence of additional diffraction peaks and the good agreement between experimental reflections and the reference stick pattern. Such behavior is commonly reported for electrodeposited PBA thin films, where kinetic growth conditions promote non-equilibrium structures with varying vacancy concentrations and compositional heterogeneity [44,45].

Due to the relatively low peak-to-background ratio and the intrinsic limitations of thin-film diffraction data, full Rietveld refinement was not performed [46]. Instead, lattice parameters were estimated from the position of the (222) reflection assuming cubic symmetry ($Fm\bar{3}m$), which provides the highest intensity and most reliable peak position across all samples. Although preferred orientation effects cannot be completely excluded, the consistent evolution of the (222) peak across the temperature series enables a reliable comparative analysis of lattice trends. This approach is commonly adopted for thin-film PBAs when peak broadening and substrate contributions limit full-pattern refinement.

The calculated lattice parameters are summarized in Table 4. For CoHCF, the lattice parameter increases from approximately 10.08 Åat 20 °C to a maximum of 10.18 Åat 40 °C, followed by a slight decrease at higher temperatures. This non-monotonic behavior indicates temperature-induced structural relaxation and framework rearrangement.

In contrast, NiHCF exhibits slightly smaller lattice parameters (10.01–10.14 Å), consistent with the smaller ionic radius of Ni compared to Co [47]. A similar non-monotonic trend is observed, with a maximum at 30 °C, suggesting that deposition temperature primarily influences defect distribution and local structural ordering rather than simple thermal expansion.

These results demonstrate that deposition temperature governs the balance between structural ordering and defect formation in PBA thin films. At intermediate temperatures, enhanced atomic mobility promotes structural rearrangement and lattice expansion, whereas higher temperatures favor defect incorporation and partial structural relaxation. The absence of peak splitting or additional reflections confirms that the cubic $Fm\bar{3}m$ structure is preserved across the entire temperature range.

When considered together with SEM and Raman analyses, the XRD results indicate that temperature-dependent compositional variations and defect redistribution control both long-range structural coherence and local structural disorder, which ultimately govern the electrochemical response of CoHCF and NiHCF thin films.

3.4. Raman spectroscopy

Raman spectroscopy was employed to investigate the temperature-dependent structural evolution of CoHCF and NiHCF thin films, with particular emphasis on the cyanide stretching region (2000–2250 cm^{-1}). This spectral range is highly sensitive to local bonding environments, oxidation states, and defect chemistry in Prussian blue analogues (PBAs) [48]. The C ≡ N stretching

Table 4
Lattice parameters of CoHCF and NiHCF thin films as a function of deposition temperature, estimated from the (222) reflection.

Temperature (°C)	CoHCF		NiHCF	
	$2\theta_{(222)}$ (°)	a (Å)	$2\theta_{(222)}$ (°)	a (Å)
20	35.81	10.08	36.04	10.01
30	35.73	10.10	35.57	10.14
40	35.45	10.18	35.62	10.13
50	35.62	10.13	36.04	10.01
60	35.46	10.17	35.89	10.05

frequency is governed by the σ-donor and π-acceptor character of the metal ions coordinated to the carbon and nitrogen termini; consequently, variations in local symmetry and compositional environment induce measurable frequency shifts [49]. Owing to this strong coupling, Raman spectroscopy provides a sensitive probe of short-range order and local structural heterogeneities – such as $[Fe(CN)_6]$ vacancies and interactions with coordinated water – which are often not detectable by diffraction techniques probing long-range periodicity. In this work, the analysis focuses on qualitative trends in band position and linewidth, which serve as indicators of temperature-dependent local structural disorder.

The most intense features appear between approximately 2000 and 2150 cm^{-1}, corresponding to the $\nu(C \equiv N)$ stretching modes of Fe – CN – M linkages. The presence of a well-defined doublet (e.g., at 2088 and 2128 cm^{-1} for CoHCF, Fig. 6(a), and 2095 and 2136 cm^{-1} for NiHCF, Fig. 6(c)) reflects the coexistence of distinct local coordination environments. These arise from variations in metal–cyanide bonding, local compositional heterogeneity, and electrostatic interactions within the PBA lattice [48]. In both systems, the low-frequency region (<600 cm^{-1}) is dominated by vibrational modes associated with Fe – C stretching and Fe – CN – M ($M = Co, Ni$) bending, confirming the preservation of the cyanide-bridged framework.

At low deposition temperatures (20–30 °C), both CoHCF (Fig. 6(b)) and NiHCF (Fig. 6(d)) films exhibit pronounced band broadening across the spectral range. This behavior indicates increased local structural disorder and reduced short-range ordering, characteristic of films formed under kinetically limited conditions. Restricted atomic mobility at low temperatures promotes rapid nucleation and the formation of small coherent domains, resulting in a distribution of Fe – CN – M bond lengths and angles. This interpretation is consistent with SEM observations of heterogeneous morphology and XRD results indicating reduced structural coherence.

As the deposition temperature increases to 40 °C, a noticeable narrowing of the Raman bands is observed, particularly in the C ≡ N stretching region. This trend is consistent with the formation of a more homogeneous cyanide framework with improved short-range ordering, driven by enhanced atomic mobility and more efficient structural rearrangement during film growth. Notably, this temperature coincides with the maximum lattice parameter obtained from XRD and the highest electrochemical response observed in CV measurements. These combined observations suggest that 40 °C represents a structural–kinetic optimum, where the expanded lattice framework is associated with improved local ordering and enhanced ion-transport pathways.

At higher deposition temperatures (50–60 °C), the Raman spectra show a subtle but systematic re-broadening of the C ≡ N stretching bands, particularly at the band edges, despite the absence of any crystallographic phase transition. This behavior indicates the emergence of additional local structural heterogeneities rather than a loss of long-range order. Elevated temperatures promote compositional fluctuations, alkali-ion incorporation, and defect redistribution, which can modify the local electrostatic environment of the cyanide ligands through mechanisms such as changes in hydrogen-bonding interactions, local symmetry distortions near defect sites, and strain fields associated with lattice rearrangements [50]. This trend is consistent with the temperature-dependent variations in the O/K ratio observed by EDS, supporting the role of compositional changes in governing local structure.

A comparison between CoHCF and NiHCF reveals that NiHCF exhibits more pronounced band broadening at elevated temperatures, indicating greater sensitivity to local structural perturbations. This behavior is consistent with differences in metal–nitrogen bonding strength and electronic configuration between Co^{2+} and Ni^{2+}, which influence the framework's tolerance to defects and compositional variations [29,35,51].

Although detailed peak deconvolution is beyond the scope of the present work, the systematic evolution of band linewidths provides robust qualitative evidence of temperature-dependent structural disorder. Overall, these results indicate that the structural evolution of CoHCF and NiHCF thin films is governed by a balance between long-range structural ordering and defect-induced local disorder. Specifically, low deposition temperatures favor heterogeneous frameworks with limited short-range order, whereas intermediate temperatures (40 °C) promote a more homogeneous cyanide network. In contrast, higher temperatures introduce composition- and defect-related distortions that broaden Raman features, despite the improved average structural ordering observed by XRD.

These local structural variations correlate with the temperature-dependent electrochemical behavior observed in CV measurements, indicating that composition- and defect-mediated structural dynamics play a key role in governing electrochemical performance in Prussian blue analogue thin films.

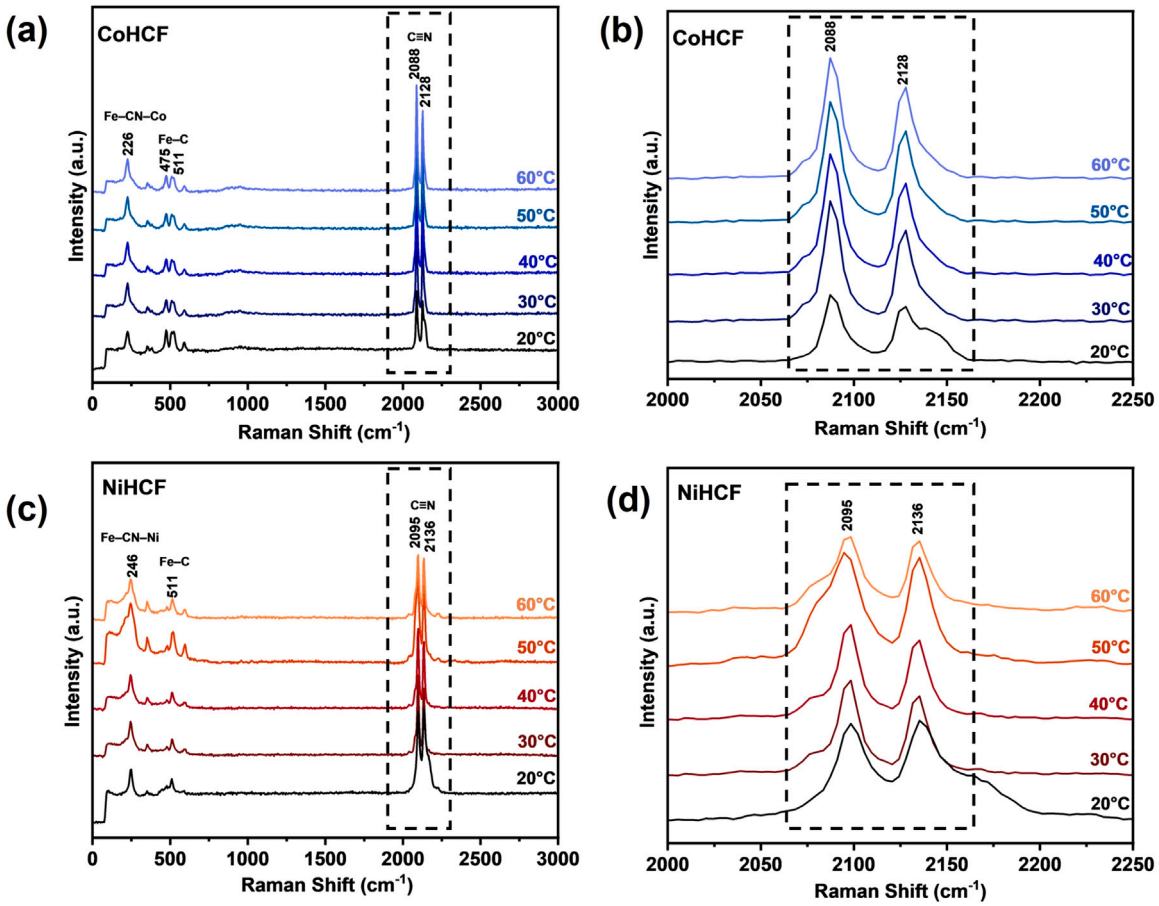


Fig. 6. Raman spectra of (a) CoHCF and (b) NiHCF thin films deposited at different temperatures. Panels (a,c) show the full spectral range, and panels (b,d) present the enlarged CN stretching region (2000–2250 cm^{-1}).

4. Conclusion

This work demonstrates that deposition temperature plays a critical role in balancing structural ordering and defect formation in Prussian blue analogues (PBAs) thin films. A clear non-monotonic relationship is observed between structural evolution and electrochemical performance, indicating that optimal ion transport is achieved by balancing framework ordering and defect-mediated transport pathways.

Quantitative comparisons based on cyclic voltammetry reveal that, under identical conditions, CoHCF exhibits approximately 2.2 times higher current densities than NiHCF, providing direct evidence of faster electrochemical kinetics. This enhanced performance is attributed to CoHCF's higher framework rigidity and lower sensitivity to defect-induced disorder.

Combined scanning electron microscopy (SEM), energy dispersive spectroscopy (EDS), X-ray diffraction (XRD), and Raman analyses demonstrate that deposition temperature modulates both long-range crystallinity and local structural environments through changes in composition, defect distribution, and hydration state. Specifically, intermediate temperatures promote improved structural homogeneity, whereas higher temperatures favor increased defect incorporation and local disorder.

These results show that the electrochemical performance of PBA thin films is not only governed by crystallinity, but also by the complex interplay of defect chemistry, lattice dynamics, and ion transport pathways. Therefore, deposition temperature emerges as a key and accessible parameter for controlling these properties.

This study provides new insights into the temperature-dependent structure–property relationships of electrodeposited PBAs and establishes a practical framework for the rational design and optimization of hexacyanoferrate-based thin-film electrodes. Notably, the results demonstrate that defect engineering, controlled by deposition temperature, is an effective method for tailoring ion transport and electrochemical functionality in cyanide-bridged materials.

CRediT authorship contribution statement

Larissa de O. Garcia: Writing – review & editing, Writing – original draft, Methodology, Investigation, Formal analysis, Data curation. **Michael Pohlitz:** Writing – review & editing. **Mohammed F. Kalady:** Writing – review & editing. **Christian K. Müller:** Writing – review & editing, Supervision, Project administration, Funding acquisition.

Funding

This work was supported by the Deutsche Forschungsgemeinschaft, Germany (DFG, Project No. 531524052) and by the European Social Fund (ESF) and the Free State of Saxony within the Landesinnovationsförderprogramm (Application No. 100670500).

Declaration of competing interest

The authors declare that they have no known competing financial interests or personal relationships that could have appeared to influence the work reported in this paper.

Acknowledgments

The authors thank Birgit Opitz from IFW Dresden for support with XRD measurements.

Appendix A. Supplementary data

Supplementary material related to this article can be found online at https://doi.org/10.1016/j.micrna.2026.208714.

Data availability

Data will be made available on request.

References

[1] K. Wu, G. Zhang, B. Yan, H. Pang, Recent progress in prussian blue analog nanomaterials: Structural engineering and functional applications, ChemSusChem 19 (1) (2025) http://dx.doi.org/10.1002/cssc.202501886.
[2] O. Javadi, S. Quick, S.O. Rastegar, Prussian blue analogues for the next-generation of beyond lithium energy storage, J. Energy Storage 141 (2026) 119244, http://dx.doi.org/10.1016/j.est.2025.119244.
[3] B. Singh, Recent advances and perspectives on prussian blue analogue-based catalysts for electrocatalytic small-molecule oxidation reactions, Coord. Chem. Rev. 552 (2026) 217546, http://dx.doi.org/10.1016/j.ccr.2025.217546.
[4] L. Duan, Z. Suo, Y. Yan, J. Zhang, R. Guo, M. Wei, H. Jin, R. Zhao, Simultaneous detection of tetracycline and kanamycin by electrochemical sensors based on dual-signal probes Au/Mn-based prussian blue analogs and methylene blue-functionalized AuPt NFs, Sensors Actuators B: Chem. 448 (2026) 138933, http://dx.doi.org/10.1016/j.snb.2025.138933.
[5] L. Shen, Y. Jiang, Y. Liu, J. Ma, T. Sun, N. Zhu, High-stability monoclinic nickel hexacyanoferrate cathode materials for ultrafast aqueous sodium ion battery, Chem. Eng. J. 388 (2020) 124228, http://dx.doi.org/10.1016/j.cej.2020.124228.
[6] S.C. Kang, N.Y. Song, S.-E. Chun, Enhancing rate performance and stability of nickel hexacyanoferrate through K+ substitution for Na+ guest ions, ECS Meet. Abstr. MA2024-02 (9) (2024) 1297, http://dx.doi.org/10.1149/ma2024-0291297mtgabs.
[7] J. Wang, P. Zhang, J. Wang, G. Huang, J. Wang, F. Pan, Improving electrochemical performance of cobalt hexacyanoferrate as magnesium ion battery cathode material by nickel doping, Batteries 11 (6) (2025) 213, http://dx.doi.org/10.3390/batteries11060213.
[8] R. Wu, B. Ren, X. Wang, J. Lin, X. Li, J. Zheng, H.Y. Yang, Y. Shang, Vacancy remediation in prussian blue analogs for high-performance sodium and potassium ion batteries, Adv. Funct. Mater. 35 (13) (2024) http://dx.doi.org/10.1002/adfm.202418018.
[9] J. Yin, J. Wang, M. Sun, Y. Yang, J. Lyu, L. Wang, X. Dong, C. Ye, H. Bao, J. Guo, B. Chen, X. Zhou, L. Zhai, Z. Li, Z. He, Q. Luo, X. Meng, Y. Ma, J. Zhou, P. Lu, Y. Wang, W. Niu, Z. Zheng, Y. Han, D. Zhang, S. Xi, Y. Yuan, B. Huang, P. Guo, Z. Fan, Unconventional hexagonal open prussian blue analog structures, Nat. Commun. 16 (1) (2025) http://dx.doi.org/10.1038/s41467-024-55775-w.
[10] D.O. Ojwang, M. Svensson, C. Njel, R. Mogensen, A.S. Menon, T. Ericsson, L. Häggström, J. Maibach, W.R. Brant, Moisture-driven degradation pathways in prussian white cathode material for sodium-ion batteries, ACS Appl. Mater. Interfaces 13 (8) (2021) 10054–10063, http://dx.doi.org/10.1021/acsami.0c22032.
[11] K. Sada, S.M. Greene, S. Kmiec, D.J. Siegel, A. Manthiram, Unveiling the influence of water molecules on the structural dynamics of prussian blue analogues, Small 20 (50) (2024) http://dx.doi.org/10.1002/smll.202406853.
[12] J. Yun, Y. Kim, C. Gao, M. Kim, J.Y. Lee, C.-H. Lee, T.-H. Bae, S.W. Lee, Copper hexacyanoferrate thin film deposition and its application to a new method for diffusion coefficient measurement, Nanomaterials 11 (7) (2021) 1860, http://dx.doi.org/10.3390/nano11071860.
[13] T. Steeger, R.L. Streng, A. Senyshyn, V. Dyadkin, X. Lamprecht, R. List, A.S. Bandarenka, Controlling the morphology and electrochemical properties of electrodeposited nickel hexacyanoferrate, ChemElectroChem 12 (13) (2025) http://dx.doi.org/10.1002/celc.202500073.
[14] J. Nordstrand, E. Toledo-Carrillo, S. Vafakhah, L. Guo, H.Y. Yang, L. Kloo, J. Dutta, Ladder mechanisms of ion transport in prussian blue analogues, ACS Appl. Mater. Interfaces 14 (1) (2021) 1102–1113, http://dx.doi.org/10.1021/acsami.1c20910.
[15] L. Avila, A. Cantudo, M. Villena, D. Maldonado, F.A. Araujo, C. Müller, J. Roldán, Variability analysis in memristors based on electrodeposited prussian blue, Microelectron. Eng. 300 (2025) 112376, http://dx.doi.org/10.1016/j.mee.2025.112376.
[16] W.-J. Li, C. Han, G. Cheng, S.-L. Chou, H.-K. Liu, S.-X. Dou, Chemical properties, structural properties, and energy storage applications of prussian blue analogues, Small 15 (32) (2019) http://dx.doi.org/10.1002/smll.201900470.
[17] W. Jiang, T. Wang, H. Chen, X. Suo, J. Liang, W. Zhu, H. Li, S. Dai, Room temperature synthesis of high-entropy prussian blue analogues, Nano Energy 79 (2021) 105464, http://dx.doi.org/10.1016/j.nanoen.2020.105464.

[18] M. Hu, J.-S. Jiang, R.-P. Ji, Y. Zeng, Prussian blue mesocrystals prepared by a facile hydrothermal method, CrystEngComm 11 (11) (2009) 2257, http://dx.doi.org/10.1039/b911613n.
[19] P.S. Camacho, R. Wernert, M. Duttine, A. Wattiaux, A. Rudola, P. Balaya, F. Fauth, R. Berthelot, L. Monconduit, D. Carlier, L. Croguennec, Impact of synthesis conditions in Na-rich prussian blue analogues, ACS Appl. Mater. Interfaces 13 (36) (2021) 42682–42692, http://dx.doi.org/10.1021/acsami.1c09378.
[20] K.M. Nair, N. Thomas, S. Pallilavalappil, S.J. Hinder, B. Brennan, S.C. Pillai, The impact of synthetic modifications on FeCo prussian blue analogue and their consequential effects on the fenton degradation of acetaminophen, J. Environ. Chem. Eng. 13 (2) (2025) 115690, http://dx.doi.org/10.1016/j.jece.2025.115690.
[21] M. Iyyappan, C. Senthil, D. Ghosh, Entropically stabilized compositionally complex prussian blue analogues in electrochemical energy storage and catalytic applications, Adv. Energy Mater. (2026) http://dx.doi.org/10.1002/aenm.202505809.
[22] G. Janani, S. Park, S. Surendran, Y. Lim, D.J. Moon, G.H. Jeong, H. Choi, G. Kwon, X. Lu, K. Jin, U. Sim, Strategic insights into prussian blue analogues-based catalysts: Design and regulation for enhanced electrochemical energy storage and conversion, Next Mater. 9 (2025) 100930, http://dx.doi.org/10.1016/j.nxmate.2025.100930.
[23] J. Sterzinger, R. Streng, S. Chen, R. Götz, W. Hu, J. Li, A.S. Bandarenka, Degradation mechanisms of prussian blue analogues and state-of-the-art approaches for stability optimization: A review, J. Phys. Chem. C 129 (15) (2025) 7135–7153, http://dx.doi.org/10.1021/acs.jpcc.5c00877.
[24] A. Abbaspour, M.A. Kamyabi, Electrochemical formation of prussian blue films with a single ferricyanide solution on gold electrode, J. Electroanal. Chem. 584 (2) (2005) 117–123, http://dx.doi.org/10.1016/j.jelechem.2005.07.008.
[25] S. Tharuman, N. Nataraj, S.-M. Chen, P. Vajeeston, B. Vellaichamy, Electrochemical sensing and catalytic water processing using cofe-PBA: Experimental and DFT insights, J. Water Process. Eng. 71 (2025) 107301, http://dx.doi.org/10.1016/j.jwpe.2025.107301.
[26] D. Weidinger, G.M. Sando, J.C. Owrutsky, Vibrational dynamics of metal cyanides, Chem. Phys. Lett. 489 (4–6) (2010) 169–174, http://dx.doi.org/10.1016/j.cplett.2010.02.070.
[27] G. Moretti, C. Gervais, Raman spectroscopy of the photosensitive pigment prussian blue, J. Raman Spectrosc. 49 (7) (2018) 1198–1204, http://dx.doi.org/10.1002/jrs.5366.
[28] M. Pohlitz, C.K. Müller, Study of growth and properties of electrodeposited sodium iron hexacyanoferrate films, Materials 15 (21) (2022) 7491, http://dx.doi.org/10.3390/ma15217491.
[29] L.d.O. Garcia, M. Pohlitz, M.F. Kalady, F. Röder, A. Lubk, D. Wolf, C.K. Müller, Electrodeposited co and Ni hexacyanoferrates: Insights into structure and morphology, Materials 18 (24) (2025) 5547, http://dx.doi.org/10.3390/ma18245547.
[30] V.D. Neff, Electrochemical oxidation and reduction of thin films of prussian blue, J. Electrochem. Soc. 125 (6) (1978) 886–887, http://dx.doi.org/10.1149/1.2131540.
[31] K. Itaya, T. Ataka, S. Toshima, Spectroelectrochemistry and electrochemical preparation method of prussian blue modified electrodes, J. Am. Chem. Soc. 104 (18) (1982) 4767–4772, http://dx.doi.org/10.1021/ja00383a001.
[32] A.V.N. Kumar, J. Joseph, Influence of co-electrodeposited gold particles on the electrocatalytic properties of CoHCF thin films, Electrochim. Acta 139 (2014) 88–95, http://dx.doi.org/10.1016/j.electacta.2014.06.156.
[33] W.A. Steen, S.-W. Han, Q. Yu, R.A. Gordon, J.O. Cross, E.A. Stern, G.T. Seidler, K.M. Jeerage, D.T. Schwartz, Structure of cathodically deposited nickel hexacyanoferrate thin films using XRD and EXAFS, Langmuir 18 (20) (2002) 7714–7721, http://dx.doi.org/10.1021/la020352e.
[34] K.M. Jeerage, W.A. Steen, D.T. Schwartz, Correlating nanoscale structure with ion intercalation in electrodeposited nickel hexacyanoferrate thin films, Chem. Mater. 14 (2) (2002) 530–535, http://dx.doi.org/10.1021/cm010156d.
[35] Y. Xu, J. Wan, L. Huang, M. Ou, C. Fan, P. Wei, J. Peng, Y. Liu, Y. Qiu, X. Sun, C. Fang, Q. Li, J. Han, Y. Huang, J.A. Alonso, Y. Zhao, Structure distortion induced monoclinic nickel hexacyanoferrate as high-performance cathode for Na-ion batteries, Adv. Energy Mater. 9 (4) (2018) http://dx.doi.org/10.1002/aenm.201803158.
[36] C.D. Wessells, S.V. Peddada, R.A. Huggins, Y. Cui, Electrochemical intercalation of sodium into prussian blue analogues, Nat. Commun. 2 (2011) 550, http://dx.doi.org/10.1038/ncomms1553.
[37] J. Joseph, H. Gomathi, G. Rao, Electrodes modified with cobalt hexacyanoferrate, J. Electroanal. Chem. Interfacial Electrochem. 304 (1–2) (1991) 263–269, http://dx.doi.org/10.1016/0022-0728(91)85509-n.
[38] H.J. Buser, D. Schwarzenbach, W. Petter, A. Ludi, The crystal structure of prussian blue: Fe4[Fe(CN)6]3· xH2O, Inorg. Chem. 16 (11) (1977) 2704–2710, http://dx.doi.org/10.1021/ic50177a016.
[39] S. Pillai, K. Dagadkhair, P.H. Salame, Electrochemical and transport properties of nickel hexacyanoferrate (KNi[Fe(CN)6]) as potential cathode material for aqueous potassium-ion batteries, Chem. Phys. Lett. 844 (2024) 141273, http://dx.doi.org/10.1016/j.cplett.2024.141273.
[40] Y. Yang, E. Liu, X. Yan, C. Ma, W. Wen, X.-Z. Liao, Z.-F. Ma, Influence of structural imperfection on electrochemical behavior of prussian blue cathode materials for sodium ion batteries, J. Electrochem. Soc. 163 (9) (2016) A2117–A2123, http://dx.doi.org/10.1149/2.0031610jes.
[41] Y. Liu, W. Chu, Y. Xu, Z. Yuan, J. Liu, H. Zhao, Q. Liu, W. Zhang, The effect of coprecipitation and heating temperature on structural evolution and electrochemical performance of iron-based prussian blue analogs, J. Solid State Electrochem. 28 (11) (2024) 4105–4118, http://dx.doi.org/10.1007/s10008-024-06005-2.
[42] Y. Waseda, The Structure of Non-Crystalline Materials: Liquids and Amorphous Solids, McGraw-Hill, New York, 1980.
[43] B.D. Cullity, S.R. Stock, Elements of X-Ray Diffraction, third ed., Prentice Hall, Upper Saddle River, NJ, 2001.
[44] A. Widmann, H. Kahlert, I. Petrovic-Prelevic, H. Wulff, J.V. Yakhmi, F. Scholz, Structure, thermodynamics, and kinetics of prussian blue, Langmuir 18 (2002) 3830–3840.
[45] B.E. Warren, X-Ray Diffraction, Addison-Wesley, 1969.
[46] R.A. Young, The Rietveld Method, Oxford University Press, 1993.
[47] J.-H. Lee, J.-G. Bae, M.S. Kim, J.Y. Heo, H.J. Lee, J.H. Lee, Effect of the interaction between transition metal redox center and cyanide ligand on structural evolution in prussian white cathodes, ACS Nano 18 (3) (2024) 1995–2005, http://dx.doi.org/10.1021/acsnano.3c08271.
[48] S.F.A. Kettle, E. Diana, E.M.C. Marchese, E. Boccaleri, The vibrational spectra of the cyanide ligand revisited: The ν(CN) infrared and Raman spectroscopy of prussian blue and its analogues, J. Raman Spectrosc. 42 (11) (2011) 2006–2014, http://dx.doi.org/10.1002/jrs.2944.
[49] K. Nakamoto, Infrared and Raman Spectra of Inorganic and Coordination Compounds, Part B: Applications in Coordination, Organometallic, and Bioinorganic Chemistry, Sixth ed., Wiley, 2009.
[50] I. Nielsen, M. Eremenko, Y. Zhang, M.G. Tucker, W.R. Brant, Local structure of hydrated and dehydrated prussian white cathode materials, J. Mater. Chem. C (2026) http://dx.doi.org/10.1039/D5TC03143E, Advance article.
[51] P. Jain, P.P. Ingole, Deciphering the synergistic effect in strong metal–support interaction toward surface reconstruction of prussian blue analogue-based pre-catalysts for boosted bifunctional oxygen electrocatalysis via operando Raman spectroscopy, J. Phys. Chem. C 128 (39) (2024) 16380–16392, http://dx.doi.org/10.1021/acs.jpcc.4c04479.